Titre: Title:	Spiderweb-inspired, transparent, impact-absorbing composite. Supplément
Auteurs: Authors:	Shibo Zou, Daniel Therriault, & Frederick Gosselin
Date:	2020
Type:	Article de revue / Article
Référence: Citation:	Zou, S., Therriault, D., & Gosselin, F. (2020). Spiderweb-inspired, transparent, impact-absorbing composite. Cell Reports Physical Science, 1(11), 100240 (17 pages). https://doi.org/10.1016/j.xcrp.2020.100240

URL de PolyPublie: PolyPublie URL:	https://publications.polymtl.ca/9279/
Version:	Matériel supplémentaire / Supplementary material Révisé par les pairs / Refereed
Conditions d'utilisation: Terms of Use:	Creative Commons Attribution 4.0 International (CC BY)

Titre de la revue: Journal Title:	Cell Reports Physical Science (vol. 1, no. 11)
Maison d'édition: Publisher:	Elsevier
URL officiel: Official URL:	https://doi.org/10.1016/j.xcrp.2020.100240
Mention légale: Legal notice:	

Cell Reports Physical Science, Volume *1*

Supplemental Information

Spiderweb-Inspired, Transparent, Impact-Absorbing Composite

Shibo Zou, Daniel Therriault, and Frédérick P. Gosselin

Note S1. Two-layer fiber fabric based on Brun et al.'s model.

Based on Brun et al.'s model described in the Experimental Procedures of the paper, we first generated the geometry of a single fiber and then manually aligned them to a 2D array in Figure S2. This way we are able to see how much the 2nd layer loops fall on top of the 1st layer loops. At a smaller speed ratio, the alternating pattern has a larger wavelength, making it easier for the 2nd layer loops to avoid falling on top of the 1st layer loops (Figure S2a). But the surface coverage of the fiber is low due to the large wavelength. At a higher speed ratio which leads to coiling pattern, the 2nd layer loops always fall on top of the 1st layer loops (Figure S2d). This will cause highly distorted fibers in the 2nd layer due to the 3D structure of the 1st layer loops in a real experiment. Therefore, we selected the alternating pattern with a wavelength as small as possible, in order to achieve a high surface coverage, as well as the fully functional sacrificial bonds and hidden lengths system in both layers.

Note S2. Static puncture test of different transparent films based on the low RI elastomer.

In order to evaluate the total energy to puncture of different specimens, we conducted the static puncture test on an electromechanical machine (MTS Insight). The puncture head diameter (25.4 mm) and the inner diameter of the annular clamp (76.2 mm) are the same as those on the impact tester. The puncture head was covered with a P60 grade sandpaper and moved at a speed of 10 mm/min. Based on the low RI elastomer (Sylgard 184), pure elastomer film, straight fiber composite film, alternating fiber composite film and hybrid fiber composite film were fabricated as mentioned in the Experimental Procedures section and all have a thickness of 1.5 mm. The specimen was clamped by two acrylic plates (thickness: 12.7 mm) and tightened by 12 screws around it to avoid slipping inside the clamps.

Note S3. Optical strain sensor based on the transparent composite from the low RI elastomer.

In the as-fabricated composite in our study, the polycarbonate core has a higher RI than the elastomer matrix, making the composite an optical waveguide with strain sensing functionality. In order to demonstrate this functionality, we used the low RI elastomer (Sylgard 184) as the matrix, and the microstructured polycarbonate fiber (printed by 1 mm nozzle) as the core. We made two different optical waveguides with the meandering fiber-elastomer composite and alternating fiber-elastomer composite.

In the sensing system (Figure S9A), a red LED was connected to one end of the waveguide. We use aluminium foils seal the connection and prevent the light from transmitting into the matrix. A photoresistor was connected to the other end of the waveguide to measure the light transmission through the meandering fiber. The resistance of the photoresistor decreases when the light intensity increases. As demonstrated by the meandering fiber waveguide in Figure S9A, when the LED is off, the photoresistor has a very large resistance (1.041 MΩ). When the LED is on and the sensor is at rest, the resistance of the photoresistor decreases to 224.5 kΩ. When the sensor is stretched by hand, the resistance further decreases to 185.0 kΩ, indicating a light transmission increase under stretching. We believe that this light transmission increase is due to the straightening of the meandering fiber, which results in less reflectance by the matrix-fiber interfaces and thus more transmittance. We further tested the sensor's repeatability through cyclic tensile test (Figure S9B). The sample was clamped with a constant force of 100N at both ends by a pair of pneumatic grips (TestResources G94). The initial gauge length was 80 mm. A cyclic displacement of 5 mm was applied at 0.017 Hz with a constant speed of 10 mm/min for a total of 105 cycles. We measured the resistance change of the photoresistor with an inverting operational amplifier (Figure S9C) and acquired the output voltage at 100 Hz by an Arduino Uno with an Adafruit SD card data logger

(Library: AnalogBinLogger). As shown in Figure S9D, the meandering fiber waveguide shows a very good repeatability under cyclic loading.

Under stretching, the alternating fiber waveguide shows a more complex behavior (Figure S9E). As explained in Figure 1C in the paper, there are four regimes during the tensile test of the alternating fiber composite. The light transmission shows a short increase during regime I, probably due to the straightening of the curved fiber segment between each sacrificial bond. In regime II, the sacrificial bonds break inside the matrix, the light path thus becomes longer and causes more reflectance and thus transmission loss. Also, the fiber detaches from the matrix, so the relative RI n^* increases from $n_{\text{fiber}}/n_{\text{matrix}} = 1.12$ to $n_{\text{fiber}}/n_{\text{air}} = 1.58$, causing more reflectance according to Fresnel's formula. In regime III, the matrix cracks and the alternating loop is unfolded, the plastic deformation of the fiber possibly further contributes to the light transmission loss. Because the alternating fiber waveguide shows a light transmission change spanning in a much larger range, we measured the resistance of the photoresistor with an electrometer (6517B, Keithley) at 50V. This test was conducted in a dark environment in order to prevent the environmental light from blocking the low transmission in the waveguide under large deformation. The transmission was calculated by $\log_{10}(I/I_0)$, where I is the measured current from the electrometer.

Under stretching, the meandering fiber waveguide and alternating fiber waveguide show a linear light transmission increase and light transmission loss, respectively. This strain sensing functionality can be integrated into the transparent impact-absorbing composite for impact protection and damage detection applications.

Note S4. Volume flow rate calibration on the Prusa 3D printer.

The theoretical volume flow rate can be calculated by the following equation:

$$Q = \frac{L_{\mathrm{E}} V_{\mathrm{F}}}{L_{\mathrm{D}}} \frac{\pi D_{\mathrm{filament}}^2}{4} \tag{Equation S1}$$

where, L_{D} is the moving distance of the printing head between the starting point and the ending point, L_{E} is the extruding length of the 1.75 mm filament from the starting point and the ending point, V_{F} is the feedrate that defines the relative moving speed of the extruder to the printing platform, the diameter of the feeding filament $D_{\mathrm{filament}} = 1.75$ mm.

The actual volume flow rate can be lower than the theoretical one due to the pressure loss. In order to measure the actual volume flow rate, we kept the L_{D} and V_{F} constant in the g-code and varied the L_{E}. For each set, eight polycarbonate fibers were produced with a deposition height of 5 mm and a 0.4 mm tungsten carbide nozzle at 330°C on the Prusa printer. We weighed the eight fibers together on an analytical balance (GH-202, A&D), and calculate the average value as the actual extruding mass M^*. Then we calculate the actual volume flow rate Q^* by the following equation:

$$Q^* = \frac{V_{\mathrm{F}} M^*}{L_{\mathrm{D}} \rho} \tag{Equation S2}$$

where, the density of polycarbonate ρ is 1.20 g/cm^3. Therefore, we obtain the volume flow rate correction factor $C_1 = Q^*/Q$ for each set (Table S2 and Figure S11).

Table S1. Comparison of the physical and mechanical properties of the low RI[1–3] and high RI[4] elastomer.

	Low RI elastomer (Sylgard 184)	**High RI elastomer (OE-6550)**
Refractive index	1.41 @589 nm	1.55 @589 nm
Viscosity (Mixed, cP)	3500	3800
Coefficient of linear thermal expansion (ppm/°C)	260 – 310[2]	210
Young's Modulus (MPa)	1.32 – 2.97[1]	5.1
Tensile strength (MPa)	3.51 – 7.65[1]	1.3
Elongation at break (%)	50 – 93[1]	75
Hardness	Shore A, 44 – 54	Shore A, 55

Table S2. Calculation of the volume flow rate correction factor C_1 for eight different printing parameter settings. Eight fibers were produced for each setting. Due to the small weight of each fiber, the eight fibers were measured together on a balance, then the weight was divided by eight to get the average value as the measured extruding mass in this table.

L_D (mm)	L_E (mm)	V_F (mm/min)	Theoretical volume flow rate (mm^3/s)	Measured extruding mass (g)	Measured volume flow rate (mm^3/s)	C_1
120	4	1929.3	2.5781	0.0119	2.6517	1.03
120	8	1929.3	5.1561	0.0206	4.6027	0.89
120	10	1929.3	6.4452	0.0253	5.6439	0.88
120	12	1929.3	7.7342	0.0293	6.5454	0.85
120	16	1929.3	10.3122	0.0383	8.5412	0.83
120	18.66	1929.3	12.0267	0.0441	9.8531	0.82
120	20	1929.3	12.8903	0.0483	10.7797	0.84
120	24	1929.3	15.4684	0.0568	12.6778	0.82

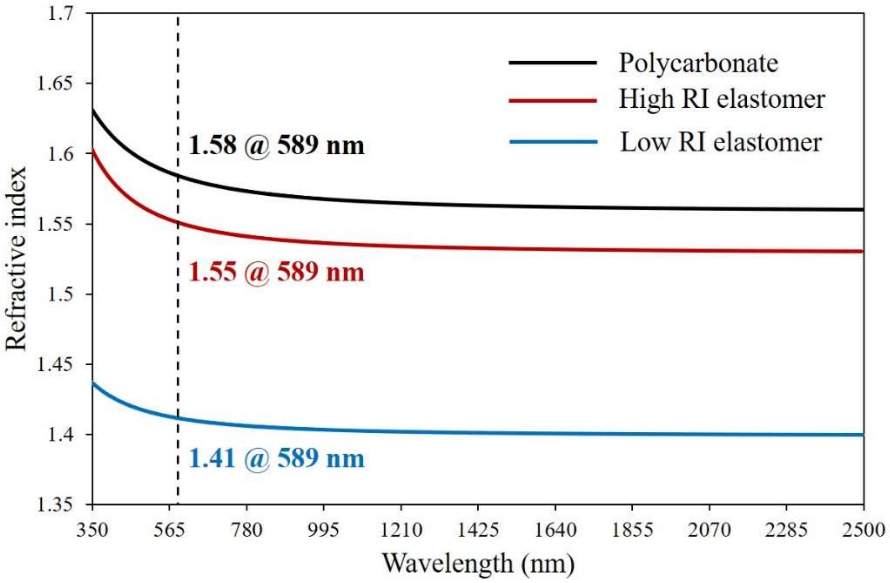

Figure S1. Ellipsometry analysis of the polycarbonate, high RI elastomer and low RI elastomer. The refractive index was obtained by the Cauchy model from 350 to 2500 nm.

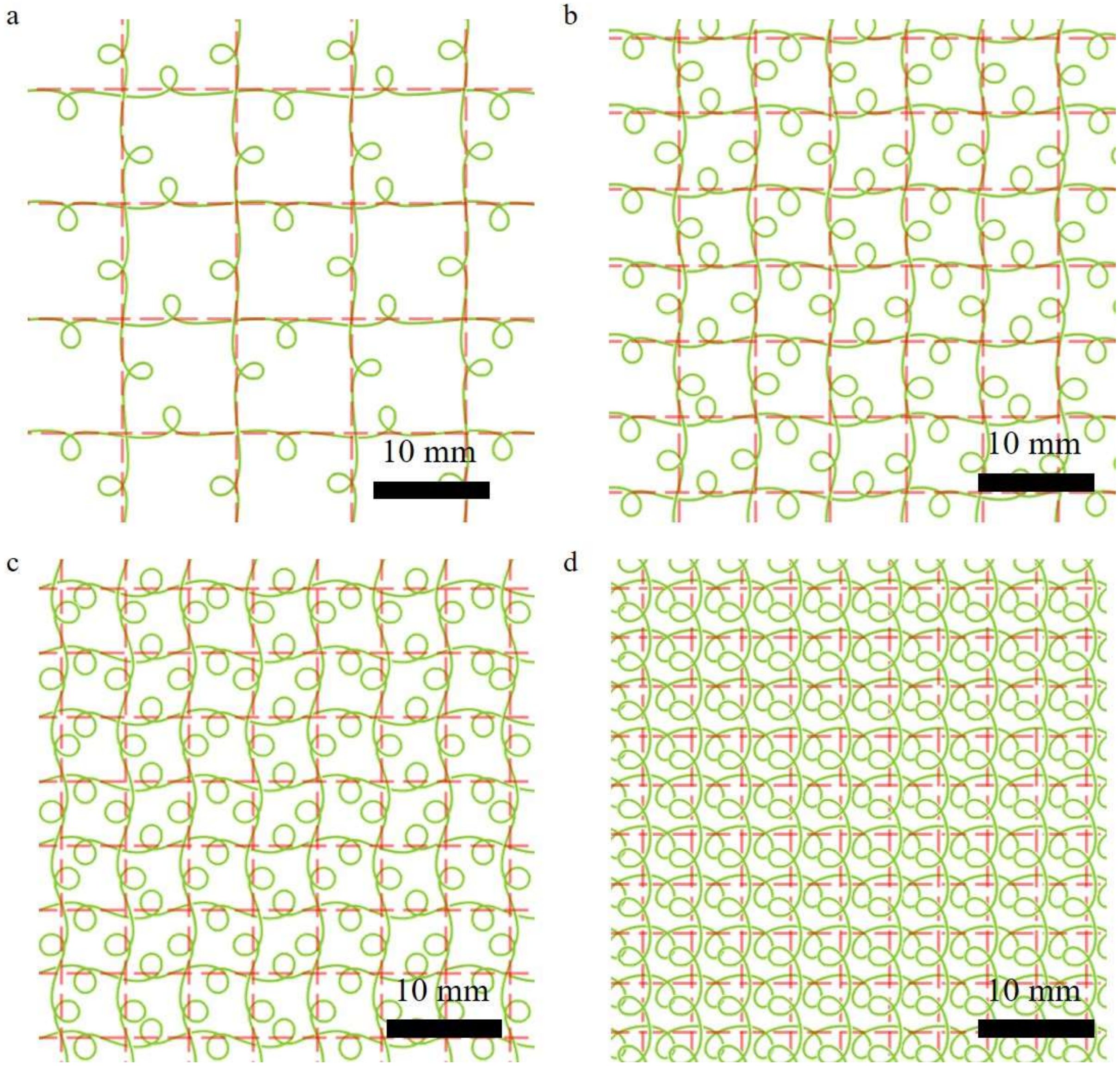

Figure S2. An ideal thought experiment of two-layer fiber fabric based on Brun et al.'s model. The single fiber pattern is generated at a speed ratio v_e/v_m =: **a**, 1.6; **b**, 1.9; **c**, 2.1; **d**, 2.4. Then the fiber was manually aligned to a 2D array (red dashed lines) with a unit size equalling to the distance between adjacent loops along the fiber. The steady coiling radius R_c = 1.8 mm was used for all calculations. The three ordinary differential equations in the model were solved via the ode23 function in MATLAB, with initial conditions $[r, \psi, \phi] = [1, 0, 3\pi/4]$.

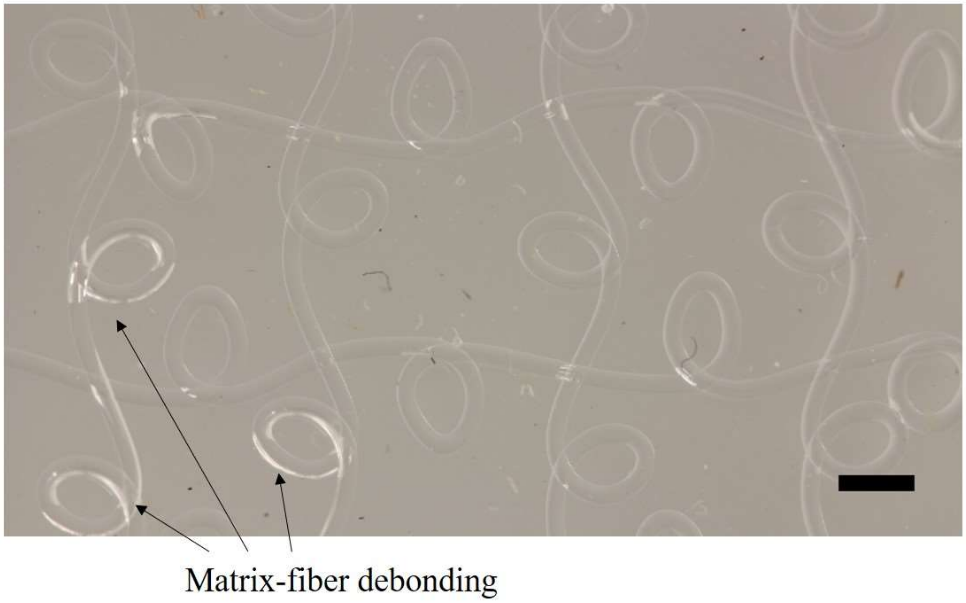

Figure S3. Matrix-fiber debonding due to thermal expansion in the alternating fiber composite film with the high RI elastomer. The composite was cured at 140 °C for 2 hours. The photo was taken after the cooling down of the composite. The scale bar is 2 mm.

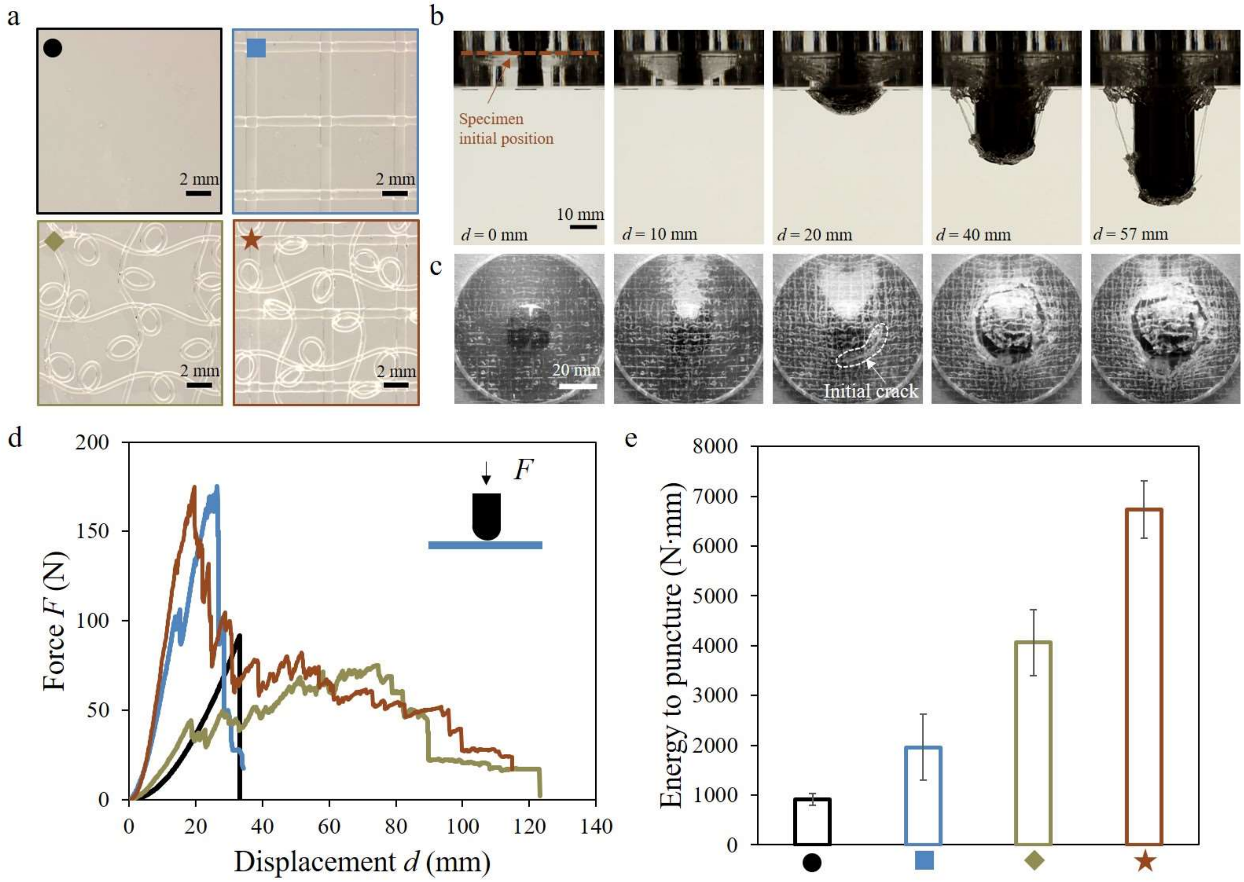

Figure S4. Static puncture test of different transparent films based on the low RI elastomer. **a**, Optical images of the pure elastomer film (black circle), straight fiber composite film (blue square), alternating fiber composite film (green diamond) and hybrid fiber composite film (red star). **b**, Front view and **c**, Bottom view of the static puncture test of a hybrid fiber composite specimen. **d**, Representative force-displacement curves for the pure elastomer film (black curve), straight fiber composite film (blue curve), alternating fiber composite film (green curve) and hybrid fiber composite film (red curve). **e**, Energy to puncture calculated by the integration of the force-displacement curve. Three repeats were conducted for each specimen, and the standard deviation was plotted as the error bar. All tests were conducted with a puncture head covered with a P60 grade sandpaper.

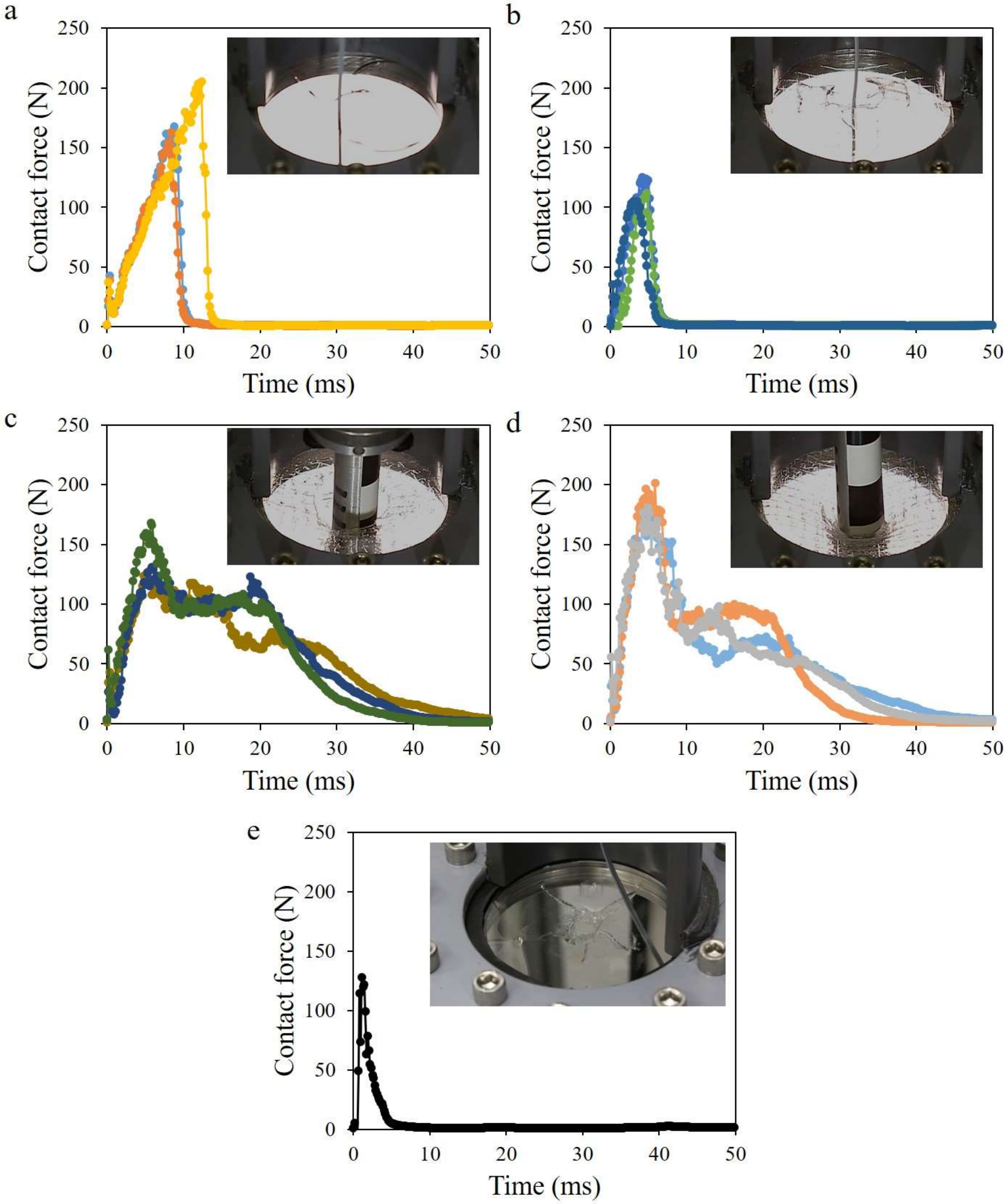

Figure S5. Contact force-time curves of different transparent films from the falling dart impact test. **a**, Elastomer film; **b**, Straight fiber composite film; **c**, Alternating fiber composite film; **d**, Hybrid fiber composite film; **e**, Polycarbonate (PC) film. The images of the films after the test are shown in the insets. The test was repeated three times in **a-d**. The dart penetrated all test films in **a** and **b**, but was successfully caught by all test films in **c** and **d**, due to the high energy dissipation of the architectured composites. All test films have a length of 100 mm and width of 100 mm. The test films in **a-d** are all based on the low RI elastomer and have a thickness of 1.5 mm. The PC film (McMaster-Carr, 85585K102) in **e** has a thickness of 0.127 mm. The weight of the test PC film is 1.524 g, which is even more than the weight of the fabric of alternating fibers (1.333 g) in **c**. The fact that the dart penetrated both the elastomer film and PC film, but was caught by the alternating fiber composite film, proves the dominating contribution from the composite architecture to the high energy dissipation over the material components.

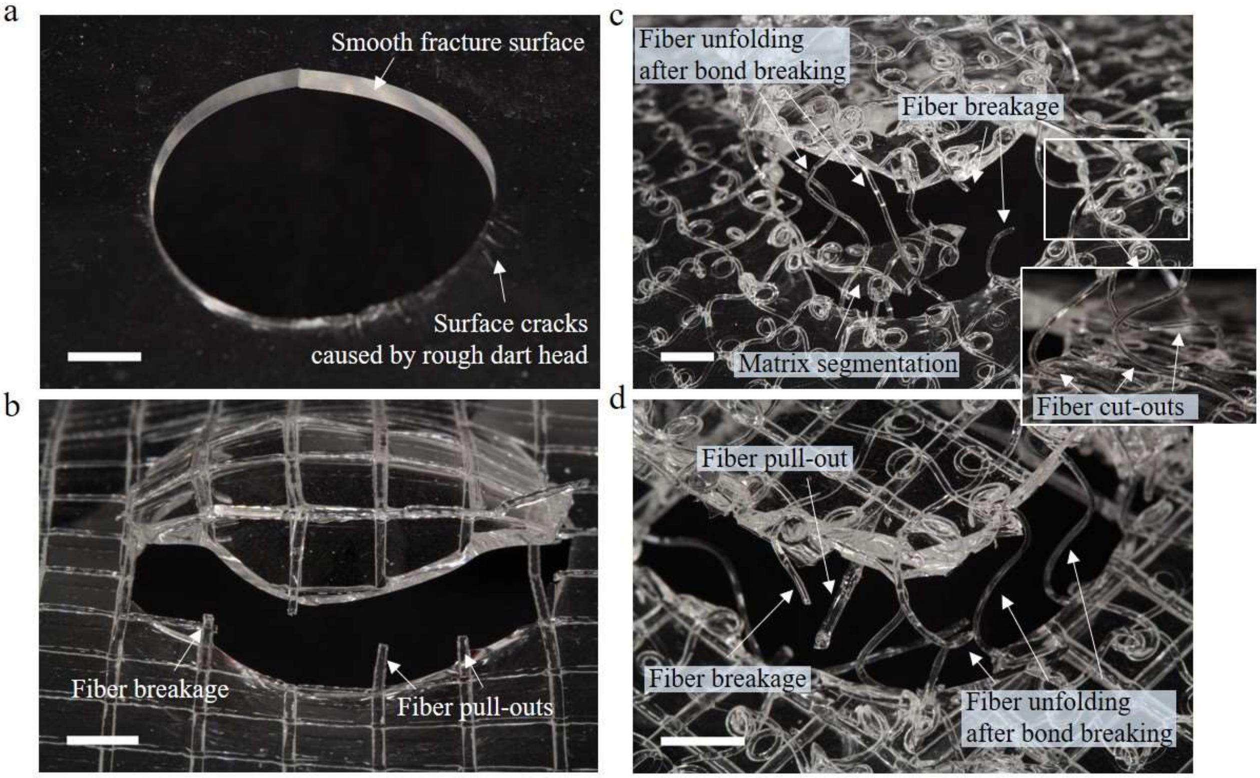

Figure S6. Optical images of fractured transparent films after impact test. **a**, Elastomer film; **b**, Straight fiber composite film; **c**, Alternating fiber composite film; **d**, Hybrid fiber composite film. The inset in **c** shows a close view of the fiber cut-outs. All scale bars are 5 mm.

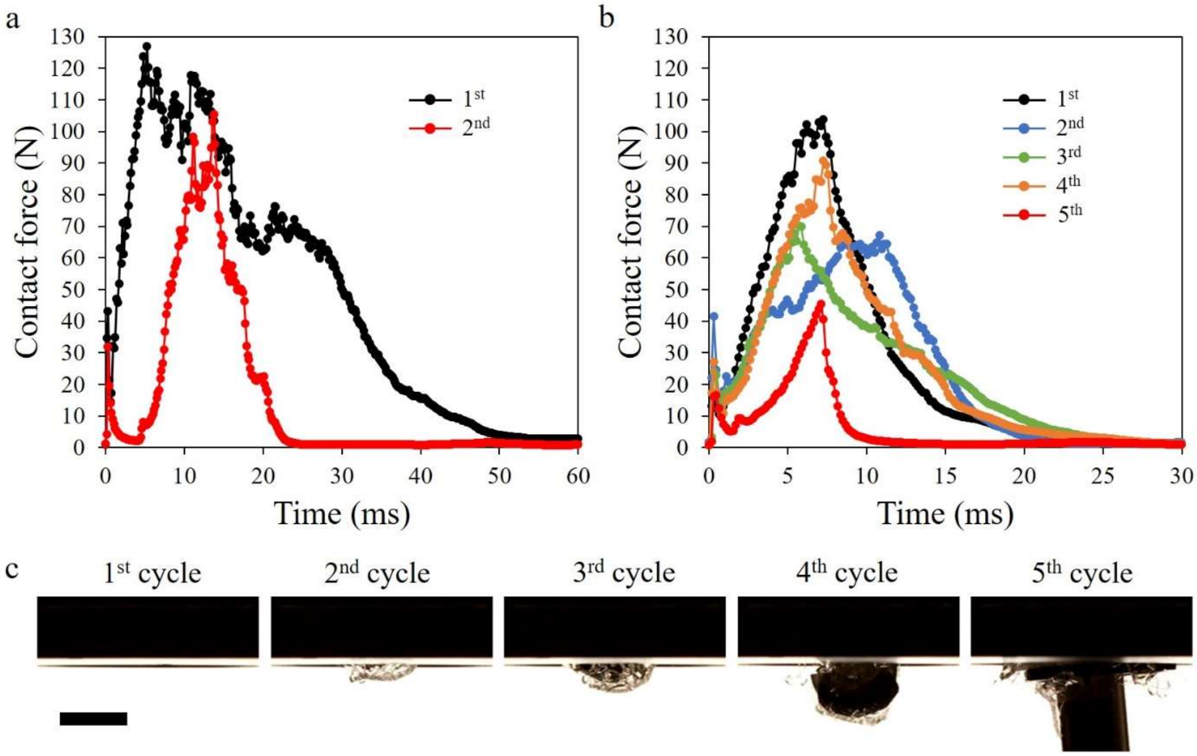

Figure S7. Cyclic impact test of the alternating fiber composite film based on the low RI elastomer. Two specimens were tested at different impact energy levels: **a**, 5 J and **b**, 1.4 J, respectively. **c**, Snapshots of the specimen at the end of each cycle of the impact test at 1.4J. For the impact test at 5J, the snapshots of the 1st cycle can be seen in Figure 4I. The same drop height (0.9 m) was used in both tests, leading to an impact velocity of 4.2 m/s. To achieve the corresponding impact energy level, the drop weight was 0.568 kg in **a**, and 0.158 kg in **b**. The drop weight fell on the same location on the specimen during the cyclic test. The drop weight fully penetrated the specimen in the 2nd cycle in **a**, and the 5th cycle in **b**. The scale bar is 20 mm.

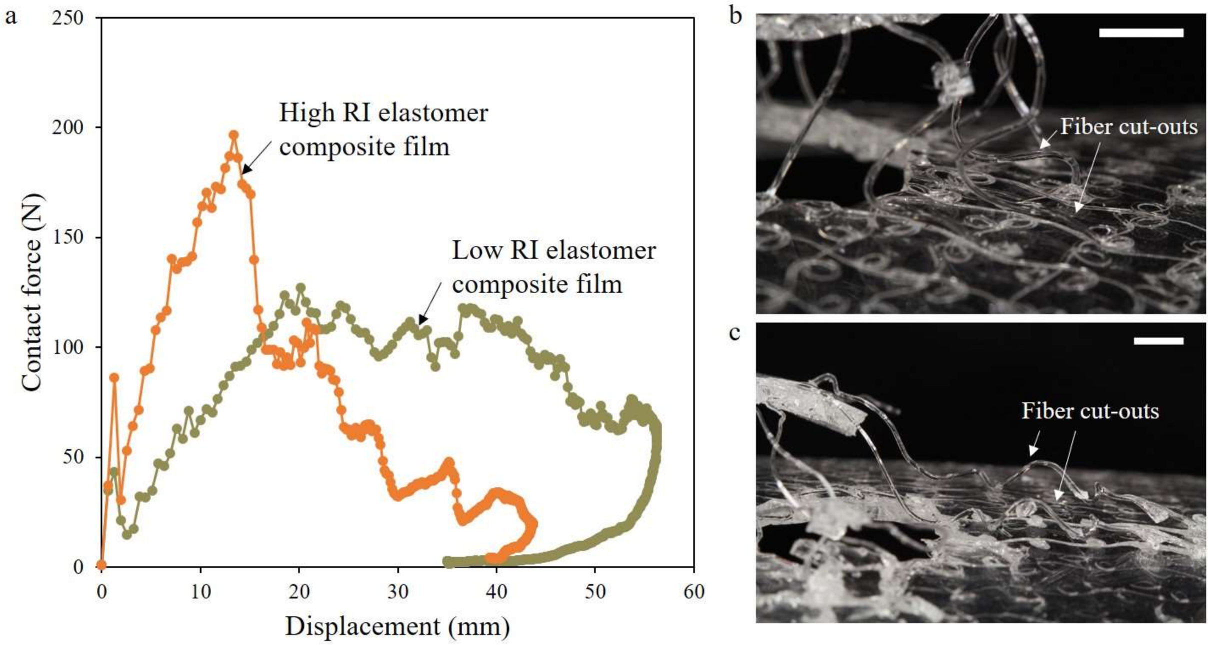

Figure S8. Comparison of the impact absorption performance between the alternating fiber composite films made from the low RI elastomer and high RI elastomer. **a**. Contact-displacement curves; **b**. Optical image of the fractured low RI elastomer composite film; **c**. Optical image of the fractured high RI elastomer composite film. Both specimens were tested with an impact energy of 5 J and impact velocity of 4.2 m/s. All scale bars are 5 mm.

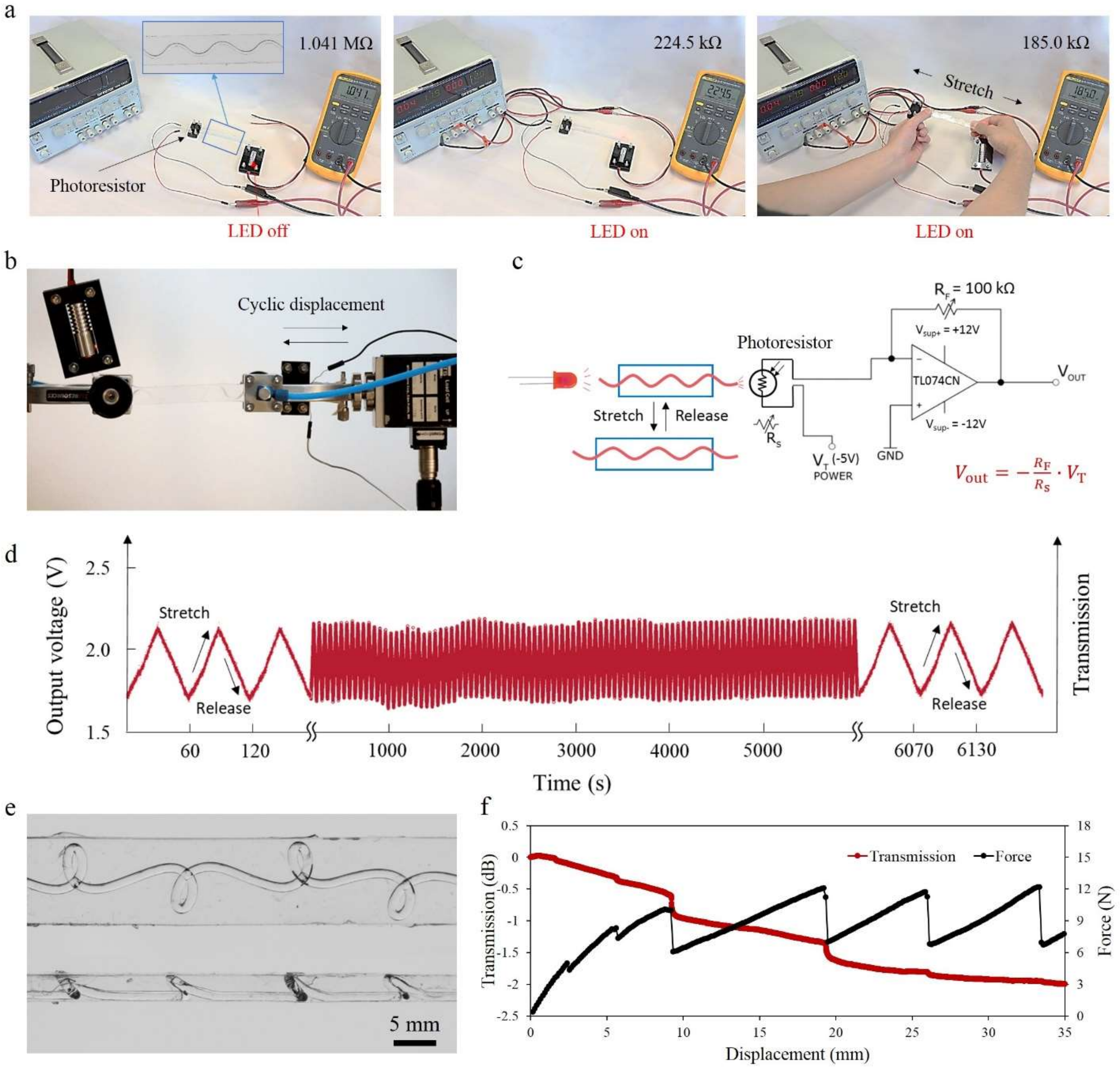

Figure S9. Optical waveguides made from the transparent composites based on the low RI elastomer. a, Demonstration of the strain sensing with the meandering fiber composite waveguide. **b**, Cyclic tensile test of the meandering fiber composite waveguide. **c**, Design of the electric circuit to measure the resistance of the photoresistor during the tensile cyclic test. **d**. Measured output voltage under the cyclic tensile test. Under stretching, more light was transmitted through the waveguide to the photoresistor, resulting in the decrease of the resistance and the increase of the circuit output voltage. **e**, Optical images (top view and side view) of the alternating fiber composite waveguide. **f**, The light transmission loss of the alternating fiber composite waveguide under uniaxial tensile test (gauge length: 45 mm; crosshead speed: 5 mm/min). The force-displacement curve is similar as Figure 1C and has been explained in the paper.

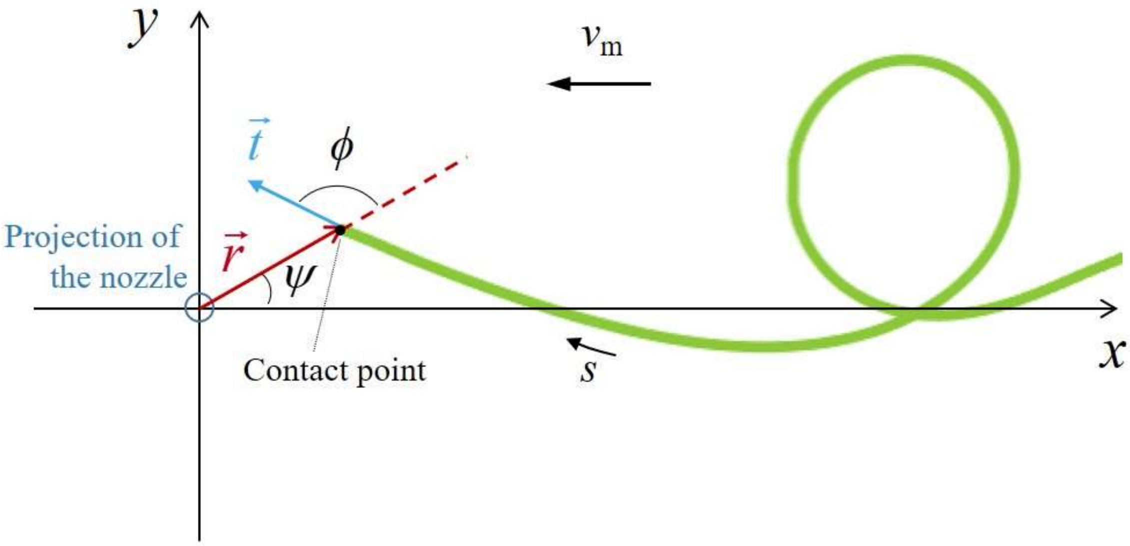

Figure S10. Schematic of the deposition trace with respect to the projection of the nozzle. The speed v_{m} is the horizontal moving speed of the extruder relative to the printing bed. The vector $\vec{r}$ represents the position of the fiber-platform contact point regarding to the nozzle's projection point. The angle ψ is measured between the vector $\vec{r}$ and the x axis (direction of the relative moving speed v_{m}). The angle ϕ is measured between the vector $\vec{r}$ and the tangent vector $\vec{t}$ of the polymer thread at the contact point. These three geometric parameters are functions of the Lagrangian coordinate s which is a time-like variable and represents the arc length along the deposition trace. The coordinates of the deposited trace can be reconstructed by the solution of the geometric model: $x(s) = r(s) \cdot \cos[\psi(s)] + v_{\mathrm{m}}(s_{\mathrm{last}} - s)/v_{\mathrm{e}}$, $y(s) = r(s) \cdot \sin[\psi(s)]$ (s_{last} is the last point from the solution). This schematic was modified from Brun et al.'s work[5].

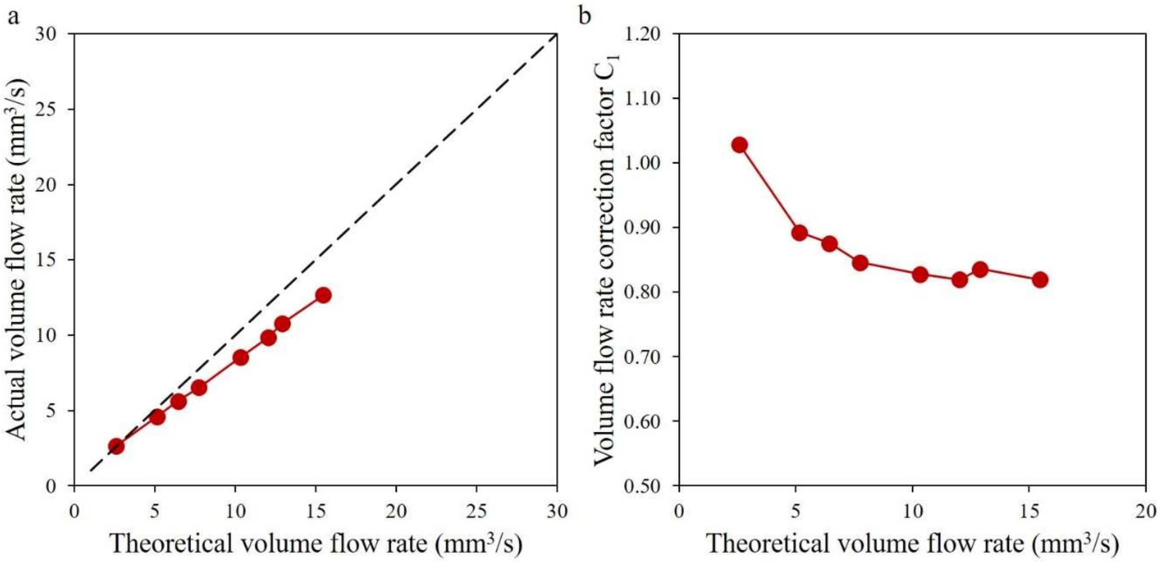

Figure S11. Calibration of the volume flow rate of polycarbonate filament on the Prusa 3D printer. The dashed line in **a** represents that the actual volume flow rate equals to the theoretical one.

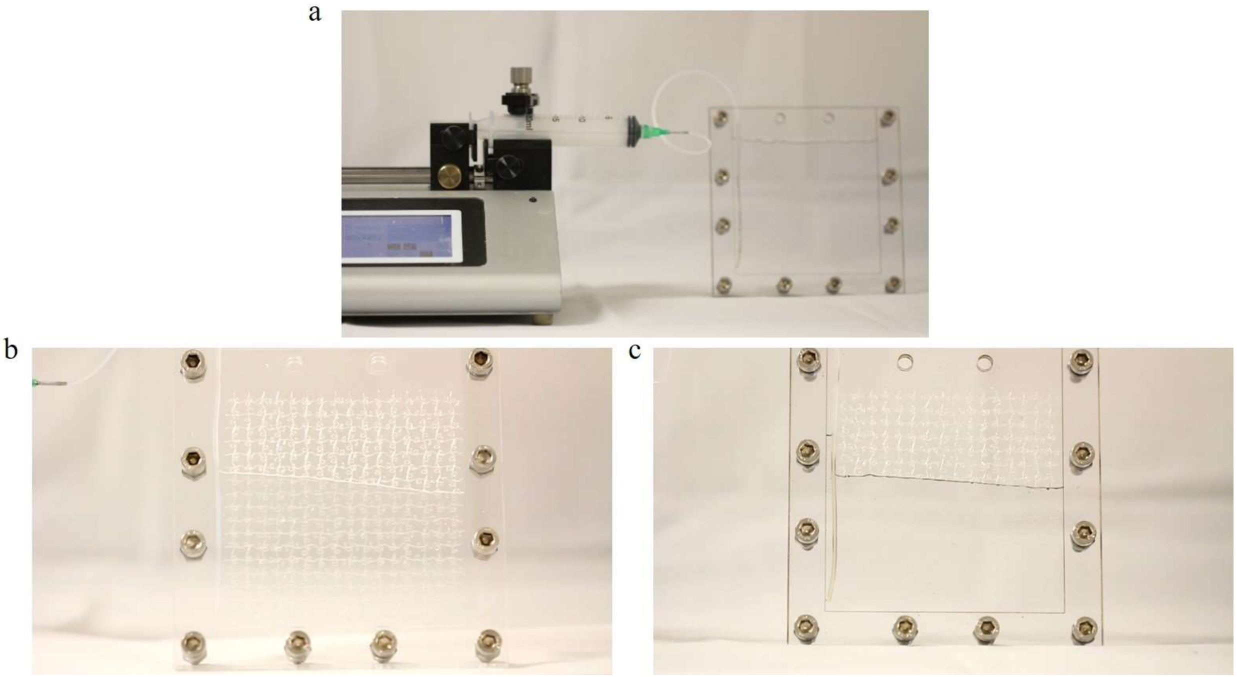

Figure S12. Resin infiltration setup. a, A micropump infiltrates the resin from the syringe into the bottom of the plastic mold via a Teflon tube. **b**, Close-up view of the infiltration process with the low RI elastomer (RI = 1.41 @589nm). **c**, Close-up view of the infiltration process with the high RI elastomer (RI = 1.55 @589nm). The alternating fiber fabric almost disappears inside the high RI elastomer resin, due to the small RI difference between the fiber (RI = 1.58 @589nm) and the high RI elastomer.

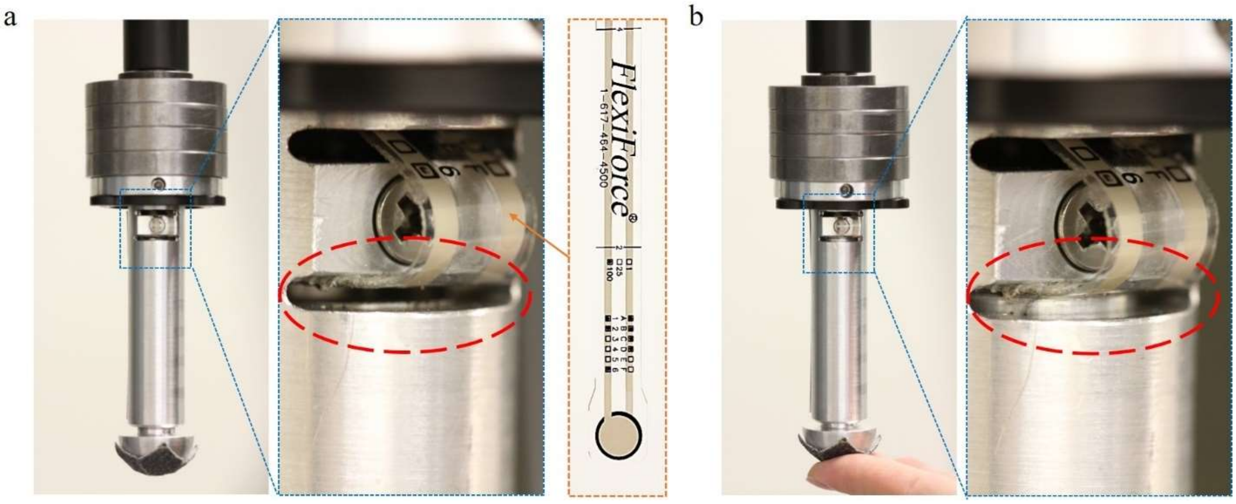

Figure S13. Design of the falling dart integrated with a force sensor. a, When the dart is overhanging, there is a gap between the force sensor and the aluminium rod inside the dart, ensuring no force is measured. **b**, When the dart is pressed, the aluminium rod will hit on the force sensor. The cross-sectional area of the aluminium rod is the same as the sensing area of the force sensor.

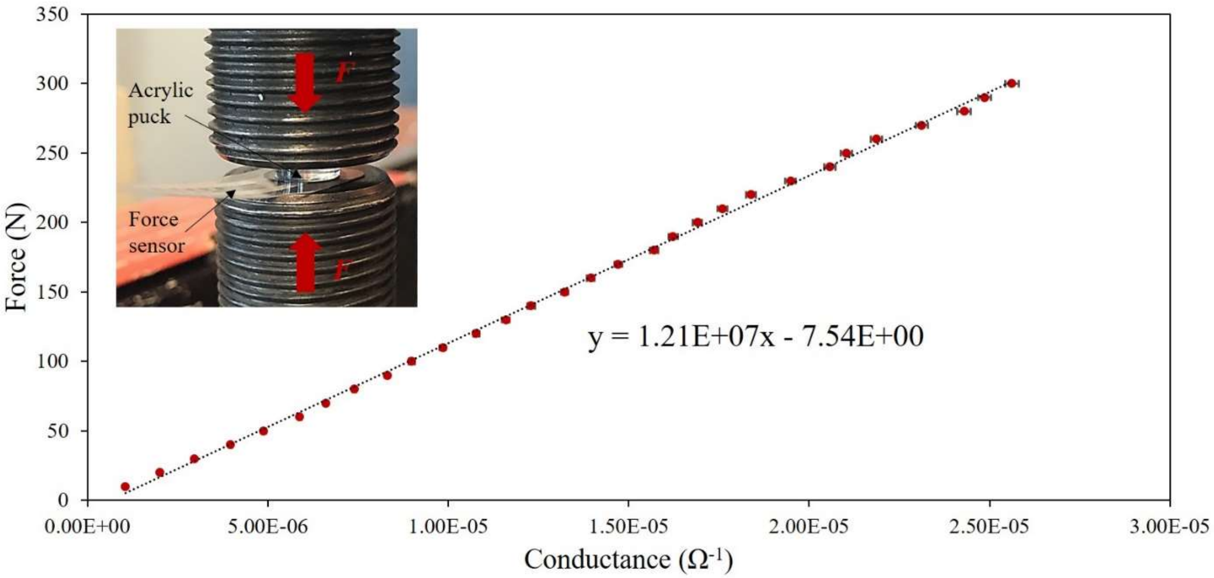

Figure S14. Calibration of the force sensor under static loading. We calibrated the sensor on an electromechanical machine (MTS Insight). The inset shows the setup. We used an acrylic puck with the cross-sectional area matching the sensing area of the force sensor. A compressive displacement was manually applied on the top clamp, until a certain force is reached. Then the conductance was measured under this force value with a digital multimeter (PCI-4070, National Instruments) and a LabVIEW program. The linear fitting was shown in the plot.

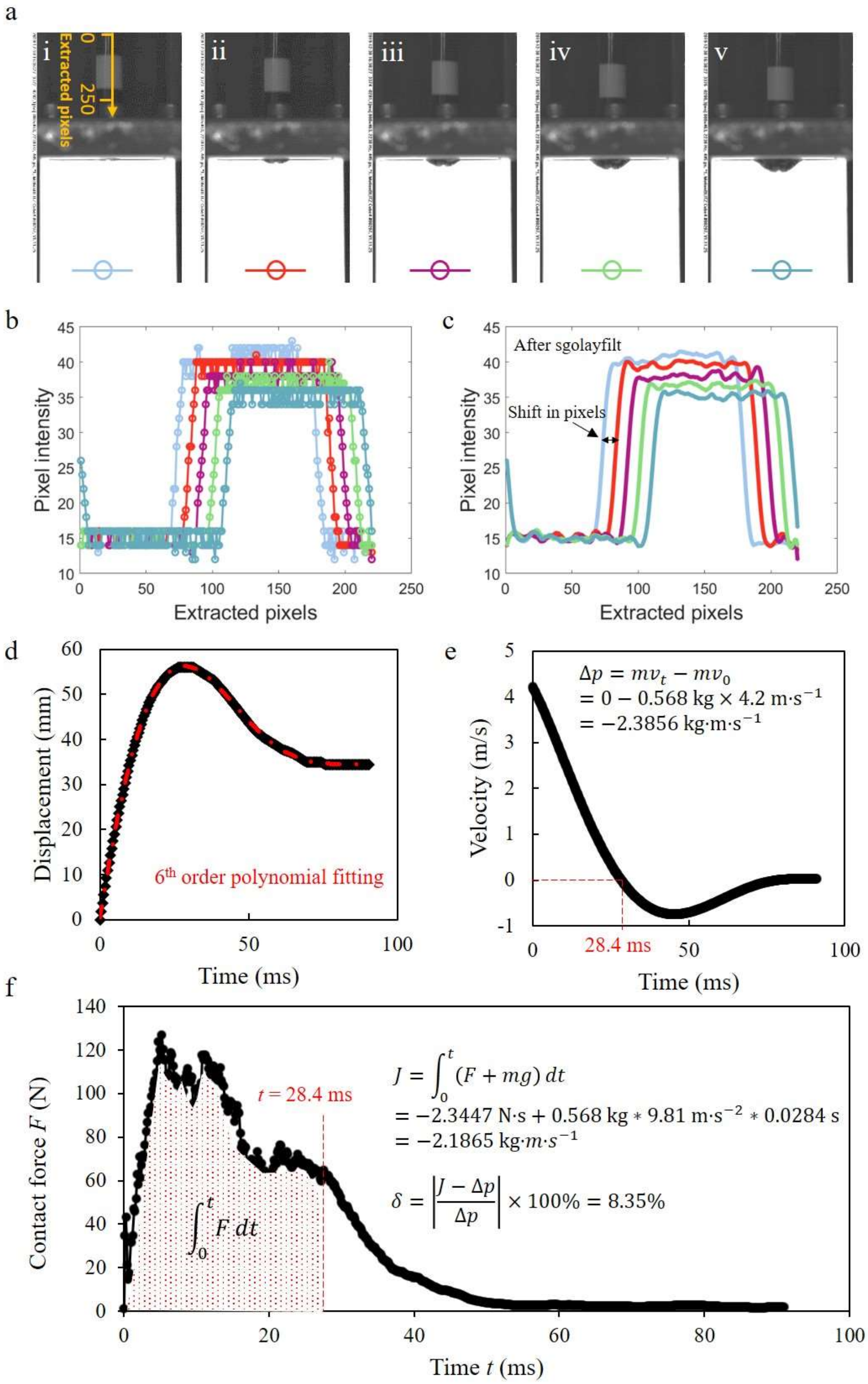

Figure S15. Displacement measurement and calibration in the falling dart impact test. a, Five consecutive high-speed camera snapshots from the impact test of the alternating fiber composite specimen. A black and white calibration paper was attached on the falling dart. **b**, The intensities of the pixels along the yellow arrow in **a** extracted by a MATLAB code. **c**, Sgolayfilt fitting of the curves in **b** with a polynomial order of 9 and frame size of 41. The MATLAB code automatically measures the shift of each curve in the unit of pixels. **d**, Displacement of the dart which is converted from the shift in pixels in **c** by the MATLAB code. The time 0 ms corresponds to the initial contact and is selected manually from the high-speed camera snapshots. **e**, Velocity of the dart which is calculated based on the 6th order polynomial fitting function in **d**. The time 28.4 ms corresponds to zero velocity. The calculation of momentum change between the initial contact and the zero-velocity time is shown in the plot. **f**, Contact force-time curve measured from the force sensor. The impulse between the initial contact and the zero-velocity time is calculated, based on the direction of gravity. The as-conducted calibration for the impact test of the alternating fiber composite specimen has a discrepancy $\delta = 8.35\%$.

References

1. Johnston, I.D., McCluskey, D.K., Tan, C.K.L., and Tracey, M.C. (2014). Mechanical characterization of bulk Sylgard 184 for microfluidics and microengineering. J. Micromech. Microeng. *24*, 035017.
2. Christopher Love, J., Wolfe, D., and Whitesides, G. (2004). Nanostructures Replicated by Polymer Molding. In Dekker Encyclopedia of Nanoscience and Nanotechnology, Second Edition - Six Volume Set (Print Version), J. Schwarz, and C. Contescu, eds. (CRC Press), pp. 2657–2666.
3. Dow Corning (2010). Dow Corning® 184 Silicone Elastomer. https://www.dow.com/content/dam/dcc/documents/en-us/productdatasheet/11/11-31/11-3184-sylgard-184-elastomer.pdf.
4. Dow Corning (2013). Dow Corning® OE-6550 Optical Encapsulant. https://samaro.fr/pdf/FT/DOW_CORNING_ELECTRONICS_FT_OE-6550.pdf.
5. Brun, P.-T., Inamura, C., Lizardo, D., Franchin, G., Stern, M., Houk, P., and Oxman, N. (2017). The molten glass sewing machine. Phil. Trans. R. Soc. A *375*, 20160156.